Supporting Information for

Supraglacial river forcing of subglacial water storage and diurnal ice sheet motion

L.C. Smith[1,2,3], L.C. Andrews[4], L.H Pitcher[5,3], B.T. Overstreet[6], Å.K. Rennermalm[7], M.G. Cooper[8,3], S.W. Cooley[9,3], J.C. Ryan[1], C. Miège[7,10], C. Kershner[11,13], C.E. Simpson[12,3]

[1]Institute at Brown for Environment and Society (IBES), Brown University, Providence, Rhode Island, 02912, USA

[2]Department of Earth, Environmental, and Planetary Sciences (DEEPS), Brown University, Providence, Rhode Island, 02912, USA

[3]Department of Geography, University of California - Los Angeles, Los Angeles, California, 90095, USA

[4] Global Modeling and Assimilation Office, NASA Goddard Space Flight Center, Greenbelt, Maryland, 20771, USA

[5]Cooperative Institute for Research in Environmental Sciences (CIRES), University of Colorado – Boulder, Boulder, Colorado, 80303, USA

[6]Department of Geology and Geophysics, University of Wyoming, Laramie, WY, 82071, USA

[7]Department of Geography, Rutgers, The State University of New Jersey, New Brunswick, 08901, New Jersey

[8]Atmospheric Sciences and Global Change Division, Pacific Northwest National Laboratory, Richland, Washington, 99352, USA

[9]Department of Earth System Science, Stanford University, Stanford, CA, 94305, USA

[10]Department of Geography, University of Utah, Salt Lake City, Utah, 84112, USA

[11]Research Directorate, National Geospatial-Intelligence Agency, Springfield, VA 22150

[12]RedCastle Resources, Inc., Salt Lake City, Utah, 84138, USA

[13]Department of Geography and Geoinformation Science, George Mason University, Fairfax, VA 22030

Contents of this file

Additional Supporting Information (Files uploaded separately)

Dataset S1: Hourly and daily summary tables of ADCP supraglacial river discharge measurements (Excel format)

Dataset S2: Hourly summary table of ADCP supraglacial river discharge measurements (text format)

Dataset S3: Hourly air temperature, melt energy and ice surface ablation computed from PROMICE KAN_M Automated Weather Station

Dataset S4: GPS-derived ice surface positions and velocity calculations

Dataset S5: Proglacial river discharge data and calculations

Dataset S6: GPS-derived and normalized discharge-difference proxies for subglacial storage (*S*) and subglacial storage change (□*S*)

Dataset S7: Time-lapse camera video of Rio Behar discharge fluctuations and ADCP data collections – 15 minute sampling (low resolution, .mp4 format)

Dataset S8: Time-lapse camera video of Rio Behar discharge fluctuations and ADCP data collections – 15 minute sampling (moderate resolution, .avi format)

Dataset S9: Time-lapse camera video of Rio Behar discharge fluctuations and ADCP data collections – 5 minute sampling (high resolution, .avi format)

Original, full-resolution data files for SonTek River Surveyor® M9 Acoustic Doppler Current Profiler (ADCP) transects and Trimble dual-frequency global positioning system (GPS) data are archived with the NSF Arctic Data Center at https://doi.org/10.18739/A22F7JS1B.
Our original GPS data files are also archived with UNVACO at https://www.unavco.org/data/doi/10.7283/GT6K-B184.

Caption for Dataset S1

Caption for Dataset S2

Caption for Dataset S3

Caption for Dataset S4

Caption for Dataset S5

Caption for Dataset S6

Caption for Dataset S7

Caption for Dataset S8

Caption for Dataset S9

Text S1: Supplemental Background

Each summer, the delivery of supraglacial meltwater to the GrIS bed causes a rapid initial rise in subglacial water pressure, which reduces basal traction and enhances ice sliding (e.g. *Zwally et al., 2002; Bartholomew et al., 2010, Hoffman et al., 2011*). A gradual slowdown in ice motion then occurs as increasing subglacial efficiency reduces regional subglacial pressure and increases basal traction (e.g. *Bartholomew et al., 2010; Hoffman et al., 2011; 2016*). Superimposed upon this seasonal cycle are short-term accelerations lasting several hours to several days attributed to variations in meltwater input (*Schoof, 2010; Andrews et al., 2014*). In the lower ablation zone, brief increases in ice speed of up to ~300% (with lesser accelerations at higher elevations) are broadly attributed to the effect of diurnal surface melting on subglacial hydrology and water pressure (e.g. *Shepherd et al., 2009; Hoffman et al., 2011; Andrews et al., 2014; Cowton et al., 2016; Davison et al., 2019*).

At a process level, however, the interaction among subglacial cavity evolution, subglacial storage, and ice motion remains difficult to interpret across spatial and temporal scales despite extensive collection of on-ice surface measurements (e.g. *Kamb, 1970; Bindschadler, 1983; Iken et al., 1983; Schweizer & Iken, 1992; Jansson, 1996; Anderson et al., 2004; Howat et al., 2008; Hoffman et al., 2011; Cowton et al., 2016; Flowers et al., 2016; Andrews et al., 2018*). GPS-derived ice surface elevations, in particular, are typically noisy and partitioning the components of uplift is uncertain. This makes interpretation of melt-induced basal uplift and uplift rates in the context of ice motion challenging (e.g. *Cowton et al., 2016; Andrews et al., 2018*). Furthermore, there is a growing appreciation that meltwater surface routing through Greenland's large supraglacial river catchments modulates the magnitude and timing of meltwater runoff entering moulins (*Smith et al. 2017; Yang et al., 2018; 2020*), which must surely influence observed variations in basal water pressure and associated ice velocity (e.g. *Zwally et al., 2002; Palmer et al., 2011; Clason et al., 2015; Banwell et al. 2016; Pitcher and Smith, 2019*). Yet, the influence of supraglacial river discharge on short-term subglacial water storage fluctuations and ice motion has received little observational study.

The purpose of this study is to examine the influence of moulin input (i.e. supraglacial river discharge) on localized, short-term accelerations in ice surface velocity. To achieve this, we explore temporal correlations between hourly time series of surface energy balance, ice ablation, supraglacial river discharge, and horizontal/vertical ice surface motion for Rio Behar, a moderately sized (~60.2 km^2 in July 2016) mid-elevation (>1200 m a.s.l.) supraglacial river catchment in the southwest Greenland ablation zone (*Smith et al., 2017*). It represents a typical catchment of the snow-free, bare ice ablation zone

(*Cooper and Smith, 2019; Ryan et al., 2019*), including intense melting and development of weathering crust development during the month of July (*Cooper et al., 2018*).

The name "Rio Behar" was first applied to this particular supraglacial river catchment in a series of Fall AGU Meeting presentations and by *Smith et al.* (2017) to honor the late Dr. Alberto Behar, who worked on our study area and died tragically 9 January 2015. We dedicate this latest research to the memory of Dr. Konrad ("Koni") Steffen, who perished on the ice sheet 8 August 2020.

The novel datasets analyzed here are: (1) 168 high-quality Acoustic Doppler Current Profiler (ADCP) consecutive hourly measurements of supraglacial river discharge (i.e. catchment runoff flux, $m^3\ s^{-1}$) acquired 6-13 July 2016 approximately 750 m upstream of the Rio Behar terminal moulin; and (2) simultaneous GPS measurements of horizontal and vertical ice surface motion (5-second sampling interval). We also use PROMICE KAN_M AWS data to estimate surface energy inputs and ablation; and compute proxies for subglacial storage (*S*) and its rate-of-change (□*S*) using both GPS and hydrographic methods. Time lapse camera images of our supraglacial river gauging site were taken every 15 minutes and compiled into a video. All of these data are freely available as tables within this SI document, as Additional Supporting Information (**Datasets S1-S8**), or from public archives (see **Data Availability**, main text).

Permanent discharge gauging stations are infeasible in the rapidly melting ablation zone environment. Owing to continuous thermal erosion of the ice bed, empirical stage-discharge rating curves rapidly obsolesce, necessitating that discharges be measured in situ rather than estimated from empirical rating curves relating occasional discharge measurements to continuously recorded water level changes. For example, in our previous study at this same field site and cross-section (*Smith at al., 2017*) we observed a ~30% error (underestimation) in rating-curve (vs. in situ) discharge retrieval within just 24 hours, due to rapid incision and changing shape of the channel cross-section. This requirement of hourly around-the-clock ADCP operations (together with non-trivial logistical challenges of camping and anchoring instruments in rapidly melting bare ice) explain the relative brevity (1 week) of our hourly supraglacial river discharge time series.

Simultaneous measurements of air temperature, radiation, and ice surface ablation were acquired from the nearby PROMICE KAN_M Automated Weather Station (*Fausto and van As, 2019*). Proglacial river discharges from two permanent gauging stations (*Rennermalm et al., 2013b; 2017; van As et al., 2017; 2019*) and one discontinued gauging station (*Tedstone et al., 2017*) were also incorporated into this study. The 60.2 km^2 July 2016 Rio Behar catchment boundary was delineated using a fixed-wing drone and

WorldView satellite imagery following the methods of *Smith et al. 2017*. This 2016 catchment boundary is presented for illustration purposes in **Figure 1**, but is not otherwise used in this study.

Text S2: Field collection and data processing of Acoustic Doppler Current Profiler (ADCP) supraglacial river discharge measurements

Over the period 5-13 July 2016, a total 847 ADCP transects were acquired at a fixed cross-section (location 67.050°N, -49.018°W) in the main-stem Rio Behar supraglacial river, using field methods based on *Smith et al.* (2017) (**Figures S1-S4**). Of these 847 transects, 677 later passed rigorous quality-assurance screening and were used to compute 174 in situ supraglacial river discharge estimates (**Tables S1-S2; Figure S5**). The 174 measurements were acquired between 13:00:09 UTC on 5 July 2016 and 10:37:57 UTC on 13 July 2016. Of these measurements, 168 were collected consecutively every hour starting 11:34:50 UTC on 6 July 2016 and ending 10:37:57 UTC on 13 July 2016. These 168 consecutive hourly measurements (1 full week) are the moulin input dataset analyzed in this study. The additional 6 discharge measurements collected intermittently on 5/6 July 2013 are excluded from our analysis because they do not fully capture the diurnal cycle, but are included in the archival dataset.

All hydrographic surveys were conducted using a SonTek River Surveyor® M9 ADCP mounted on a SonTek HydroBoard II and a moving-boat survey type. To complete each survey, the M9 system was towed, in-transect, back and forth across the Rio Behar Channel, using a custom bank-operated cableway that enabled single-side tensioning and operation (**Figures S1-S4**). Between 3-9 individual hydrographic profiles or transects of channel cross-section, wetted perimeter, and flow velocity were collected during each measurement hour, yielding a total of 847 transects acquired over the field experiment study period (**Tables S1-S2, Additional Supporting Information Datasets S1-S3**)

ADCP data were later processed into high-quality discharge retrievals using the following quality assurance (QA) and quality control (QC) workflow. This QA/QC workflow is similar to that described in *Smith et al.* (2017) and consists of the following:

1. Open all ADCP output files for a given hour in River Surveyor Live (RSL) software and manually check/edit system settings. For all files, the Transducer depth was set to 0.1 m, the magnetic declination was set at -29, GPS reference was set to

GGA, and the depth reference was set to Vertical Beam (VB) (rather than Bottom Track, BT).

2. Instrument performance was also validated in RSL. Our system quality checks include: ensuring system power or voltage >9.5, GPS quality >= 3, Horizontal Dilution of Precision (HDOP) <= 2, the track reference was >0. Quality checks were initially conducted manually, and were later automated using Matlab.
3. The edge or bank data for each measurement were manually inspected to confirm that the ADCP was receiving velocity and depth data near the profile edges. Profiles with no edge data (for either or both edges) were discarded from the final hourly discharge estimate.
4. The depth data for each profile were inspected by comparing both the VB and BT data series and determining which depth reference was higher quality (i.e. had fewer outliers and less dropout). If both VB and BT were of equal quality, VB was selected as the depth reference. If VB had substantial dropout or anomalies, BT was selected. If either VB or BT had data dropout whereas the other depth reference contained data, composite tracks were selected such that RSL fills gaps in depth data series. Each profile was manually ranked on a scale from 0 to 3, where 0 or 1 indicates a poor or unusable transect due to insufficient depth data, 2 indicates a profile with minimal outliers and dropout, and 3 indicates a profile with no outliers or dropout. Profiles ranked as 0 or 1 were discarded from the final hourly discharge estimates, unless all transects in a given measurement hour were ranked as 0 or 1. In this instance, all transects were kept unless certain transects had notable more outliers or data dropout than other transects, in which case lower quality transects were removed from the final hourly discharge estimate.
5. Velocity vectors and the signal-to-noise ratio were also inspected manually. Velocity vectors were ranked on a scale of 1 to 3, where 1 indicates minimal perpendicular vectors, substantial drift, or no data, 2 indicates vectors with moderate drift and some vector crossover, and 3 indicates minimal to no drift or crossover. Profiles with a ranking of 1 were discarded from the final hourly discharge estimate.
6. All QA/QC'd data files were exported from River Surveyor Live as Matlab files. Both original ADCP data files (.riv or .rivr) readable in River Surveyor Live (which can be freely downloaded from the SonTek/Xylem website after registering with an email address) and Matlab format outputs are now archived with the Arctic Data Center at https://doi.org/10.18739/A22F7JS1B.

7. Following manual/automated QA/QC checks, resultant ADCP data and associated variable descriptions were summarized for each measurement hour. These summary data are presented in **Tables S1-S2**; and in as **Additional Supporting Information** in Excel spreadsheet (**Dataset S1**) and .txt (**Dataset S2**) formats.

Text S3: Description of variables for full-resolution ADCP datafiles

Sample filename: RioBehar16_adcpQ_hourly_20190731.txt

Variables:

- 'measHr' = measurement hour. Data values range from -6 to 167. We measured discharge (Q) hourly a total of 174 times (of which 168 were continuous hours and analyzed in this study) from 5-13 July 2016, beginning 13:00:09 UTC on 5 July 2016 and ending 10:37:57 UTC on 13 July 2016. The continuous 168 hour record starts at measHr = 0 (11:34:50 UTC on 6 July 2016) with the 6 non-continuous measurements collected prior to measHr = 0 noted as negative measHr values.
- 'startYear' = year at measurement start
- 'startMonth' = month at measurement start
- 'startDay' = day of month at measurement start
- 'startHour' = UTC hour at measurement start
- 'startMinute' = UTC minute at measurement start
- 'startSecond' = UTC second at measurement start
- 'endYear' = year at measurement end
- 'endMonth' = month at measurement end
- 'endDay' = day of month at measurement end
- 'endHour' = UTC hour at measurement end
- 'endMinute' = UTC minute at measurement start
- 'endSecond' = UTC second at measurement start
- 'nFiles' = number of ADCP profiles collected during a measHr
- 'nGood' = number of ADCP profiles flagged as good or usable during QA/QC for a measHr
- 'avgQ' = average of all usable ADCP profiles for a measHr. Units = $m^3 s^{-1}$'medQ' = median of all usable ADCP profiles for a measHr. Units = $m^3 s^{-1}$
- 'minQ' = minimum of all usable ADCP profiles for a measHr. Units = $m^3 s^{-1}$
- 'maxQ' = maximum of all usable ADCP profiles for a measHr. Units = $m^3 s^{-1}$
- 'std' = standard deviation of all usable ADCP profiles for a measHr.
- 'range' = range of all usable ADCP profiles for a measHr. Units = $m^3 s^{-1}$
- 'startUtc' = measurement start date and time in UTC stored as .mat datetime variable

- 'endUtc' = measurement end date and time in UTC stored as .mat datetime variable

Text S4: Field collection and data processing of GPS ice surface motion measurements

Records of positional location were collected with a Trimble R7 dual-frequency global positioning system (GPS) receiver and Trimble Zephyr Geodetic antenna (**Figure S6**). The system was installed ~750 m SSE of the moulin near the ADCP gauging site at location 67.048°N, -49.018 °W, elevation 1211.43 m) The antenna was affixed to a 3.3 m schedule-40 aluminum rod drilled vertically 3 m into the ice. The aluminum rod-antenna setup was allowed to freeze overnight. The system was powered by a 40 W solar panel attached to a weatherproof Pelican hard case that enclosed the GPS receiver, batteries, and cables adjacent to the antenna. The ice sheet thickness at this location is ~934 m based on Bedmachine v3 (*Morlighem et al., 2017*). The entire system was provided by UNAVCO (formerly University NAVSTAR Consortium), with protocols for field installation and GPS receiver settings provided by UNAVCO geodetic support engineers. The GPS station recorded positions at 5-s intervals between 5 and 13 July 2016. A base station was also established on bedrock near the ice sheet terminus (67.150°N, 50.058°W, elevation 581.19 m) and recorded positions at 5-s intervals between 4 and 15 July 2016.

Trimble binary receiver files were converted to RINEX observation files using runpkr00 v5.40 and TEQC utilities (*Estey and Meertens*, *1999*). On-ice kinematic GPS positions were estimated using carrier-phase differential processing relative to the bedrock mounted reference station (baseline of ~47 km) using TRACK v1.28 (*Chen*, 1998) and final International GNSS Service satellite orbits following *Hoffman et al. 2011* and *Andrews et al., 2018*. During processing, kinematic station motion was constrained on an epoch-by-epoch basis to 2,000 m yr^{-1} to permit rapid, short-term velocity changes. The 5-s time series was then smoothed with a 6-hr phase-preserving boxcar filter to eliminate spurious signals associated with GPS uncertainties and decimated to a 15-min time series. The smoothed x and y positions were used to calculate 6-hr velocities using a centered time window to limit aliasing that may result from using discrete time intervals. Uncertainties presented here are +/- one standard deviation of the 15-min binned 5-s position data.

In several instances, we use daily peak values as part of our analysis, these peaks are identified using Matlab `findpeaks`. As part of this processing, we assess the timing, magnitude, and normalized peak prominence of GPS-derived ice speed and detrended surface elevation (**Table S3**). To calculate normalized peak prominence, we first normalize each dataset between 0 and 1, and then measure the prominence of the peak relative to the surrounding data. A value closer to 1 indicates that the peak in the dataset is clear and prominent, while a value closer to 0 indicates that the peak may be obscured or difficult to identify from the surrounding data. Detrended surface elevation has the lowest peak prominence.

Text S5: PROMICE KAN_M Automated Weather Station data and processing

Hourly weather station data were downloaded for the PROMICE KAN_M automated weather station (AWS; *Fausto and van As, 2019*, available at https://www.promice.org/PromiceDataPortal/). The KAN_M AWS is located just outside the 2016 Rio Behar catchment (**Figure 1**) and is also used in *Smith et al.* (2017). This station, operated by the Geological Survey of Denmark and Greenland, records a range of surface atmospheric variables and ice conditions. Here we use hourly mean energy balance components, surface air temperature and surface ablation measurements to examine the relationship between atmospheric forcing and ice sheet motion. The hourly melt energy (**Figure 2a**) is calculated by summing the net longwave radiation, net shortwave radiation, sensible heat flux and latent heat flux. The shortwave radiation is corrected for any sensor tilt recorded. Sensible heat flux is calculated from the wind speed and temperature gradients between the surface and the sensor height, with an assumed aerodynamic surface roughness of 0.001 m. Latent heat flux is calculated from the wind speed and humidity gradients between the surface and sensor height using the same aerodynamic roughness prescribed for sensible heat flux. Air temperature is presented as recorded by the AWS. Ice surface ablation is calculated by differencing the hourly observations of the pressure transducer (drilled into the underlying ice) every 6 hours. During the observation period, the pressure transducer remained fully embedded within the underlying ice and did not need to be reinstalled.

As part of this processing, we assess the timing, magnitude, and normalized peak prominence of weather observations (**Table S3**). Normalized peak prominence is calculated as described in **Text S4**. Melt energy has the highest normalized peak prominence. The same process is also performed for Watson proglacial discharge (**Text S6; Figure 3; Table S3**).

Text S6: Proglacial river discharge data and processing

Hourly proglacial discharges for Qinnguata Kuussua/Watson River (*van As et al., 2017; 2019*) were downloaded from https://doi.org/10.22008/promice/data/watson_river_discharge. Proglacial discharges have been recorded at this location since 2006, using in situ pressure transducer measurements of stage (water level) and an empirical stage-discharge rating curve calibrated with intermittent in situ discharge measurements acquired from different techniques including current meters, float method, and Acoustic Doppler Current Profiler (ADCP) transects. These discharge estimates have an estimated 15% uncertainty due to rating curve fit and errors in cross-sectional area and velocity measurements (*van As et al. 2017*).

Hourly proglacial river discharges in Akuliarusiarsuup Kuua, a major headwater tributary of Qinnguata Kuussua/Watson River ~33 km upstream of the Kangerlussuaq bridge and just ~2 km downstream of the ice edge, were downloaded from https://doi.org/10.1594/PANGAEA.876357. Proglacial discharges at Akuliarusiarsuup Kuua have been recorded since 2008 at a road bridge crossing (AK4 station, *Rennermalm et al., 2013b; 2017*). Stage and water temperature data are collected every 30 minutes using a Solinst® Levelogger pressure transducer and atmospheric barometric pressure logger (accuracies 0.003 m and 0.05°C for the Levelogger, and 0.001 m for the barologger, respectively). Discharges are estimated from the continuously recorded stage data using an empirical stage-discharge rating curve calibrated by periodic in-situ discharge measurements collected from the bridge, using either USGS-style Price AA current meters or a SonTek River Surveyor® ADCP.

Sub-hourly proglacial river discharge measurements from the Leverett Glacier (*Tedstone et al., 2017*) were downloaded from https://ramadda.data.bas.ac.uk/repository/entry/show/?entryid=17c400f1-ed6d-4d5a-a51f-aad9ee61ce3d. These measurements were collected at a stable bedrock section (67.06°, -50.22°) approximately 2 km downstream from the Leverett Glacier terminus between 2009 and 2012 (e.g., *Bartholomew et al., 2011; 2012*). Depending on the year, river stage measurements were logged every 5-10 minutes. These time series are converted to discharge with an estimated uncertainty of ±15%, using season-specific ratings curves developed from intermittent dye-dilution gauging experiments (*Bartholomew et al., 2011*).

The volume and timing of subglacial water emerging at the ice edge is sensitive to subglacial water pressure (e.g. *Armstrong and Anderson, 2020*). Therefore, to appropriately examine the relationship between regional subglacial water storage, ice motion and proglacial discharge, we need spatially integrated measurements of proglacial discharge collected along the ice sheet edge. Unfortunately, we must utilize non-ideal data. Here, our approach is to correct Qinnguata Kuussua/Watson River discharge measurements collected at Kangerlussuaq bridge (*van As et al., 2017; 2019*) to be representative of proglacial discharge emerging along the ice sheet edge. This approach has the benefit of providing a picture of proglacial outflow from a larger area of the ice sheet than AK4, maximizing the likelihood of subglacial linkage to Rio Behar moulin, despite uncertain basal routing in the region (e.g. *Lindbäck et al*., 2015), while also reasonably adjusting the hydrograph to remove the time associated with water transit and/or wave celerity between the terminus and Kangerlussuaq (e.g. ~33km from the Russell Glacier). To estimate the timing of peak daily discharge along the ice edge using these data, we perform a series of steps to assess the peak timing difference between the Watson River station, AK4 station, and the Leverett station. Finally, we perform a second, stand-alone analysis using AK4 station data only (**Figure S13, Figure S14, Table S5**), which does not require use of a proglacial timing delay correction.

First, we assess discharge peak timing for the Watson River station, AK4 station, and the Leverett station during the month of July between 2009 and 2011 (**Figure S7**). We exclude available July 2012 measurements because a large melt event (e.g., *Tedesco et al., 2013*) produced a highly variable and difficult-to-discern diurnal signal dissimilar from other years and from 2016. To enable uniform comparison among these three proglacial discharge datasets we linearly interpolate the Leverett and AK4 station data to 1 hour to match the Qinnguata Kuussua/Watson hydrograph data. We also apply a Lowess filter with a smoothing factor of 0.02 to the Leverett hydrograph to reduce noisiness. This smoothing enhances identification of daily peaks while also preserving their timing. To identify daily peaks, we subtract the 24-h running mean and use the Matlab `findpeak` function to extract peak timing (**Figures S8-S10**).

Next, we find the best approximation of the mean time differences between diurnal discharge peaks among all three stations between 2009 and 2011. To do this, we calculate the daily difference between Qinnguata Kuussua/Watson and Leverett and Watson and AK4. The distribution of the timing difference for both discharge pairs is nearly normal and centers on a -5h delay between the ice edge and Kangerlussuaq (**Figure S9**). These values change slightly to -5.1h±1.7 for Watson-AK4 and -4.8h±2.3h for Watson-Leverett with an additional significant figure. We conclude that on average, daily peak discharge at Kangerlussuaq bridge lags both Leverett and AK4 by ~5h with a standard deviation of 2h, considering appropriate significant figures, for all days in July over the period 2009-2011. Importantly, these additional analyses demonstrate that the timing of peak daily discharge is essentially synchronous for AK4 and Leverett, thus affirming regional representativeness of the AK4 station.

Finally, we assess the peak timing difference between Kangerlussuaq and AK4 immediately before and during our observation period (1-16 July 2016) to ensure that the difference falls within the range expected from the 2009 to 2011 data measured at Leverett and AK4 (**Figure S10**). We find a slight timing difference between the 2009-2011 and 2016 observations (-6h ±1h). However, we also note that the 2016 data are not normally distributed and the most frequent timing differences are -5h. Furthermore, the median timing difference for both the 2009-2011 and 2016 data is -5h. Therefore, we apply a fixed -5h correction to the Watson River dataset to correct for the timing offset between peak daily flow at the regional ice edge versus peak daily flow at the Kangerlussuaq bridge. While this adjustment can be influenced by host of uncertainties, we feel that examination of multiple years of data at three different proglacial gauging stations results in an accurate assessment of this timing offset between the terminus and the Kangerlussuaq gauging station. We include a sensitivity analysis using the standard deviation, 2h, to assess the potential impact of routing delay variations on our primary findings (see **Text S8** and **Figure S12**). While we use this corrected proglacial discharge hydrograph for all analyses (e.g. **Figure 2, Figure 3, Figure 5**), we also remove the hydrograph's immediate linear trend when examining the lagged correlation between proglacial discharge and ice speed, in order to eliminate the potential for autocorrelation (i.e. detrended proglacial data in **Figure 4f, Figures S8-S10, Tables S3-S4**).

Note that this -5h proglacial correction is not the same thing as a proglacial flow routing delay because it does not distinguish between wave celerity and Lagrangian flow. However, it is sufficient for our purpose here, which is simply to estimate the daily timing of peak proglacial outflow occurring at the ice edge using measurements acquired at Kangerlussuaq. Furthermore, note that this -5h proglacial timing correction does not represent the time difference between peak daily discharge entering Rio Behar moulin and peak daily discharge at the ice edge. Cross-correlation analysis between daily peaks in moulin input and estimated daily proglacial discharge peaks at the ice edge indicate a mean timing difference (again, timing difference only, not routing time) of ~1h, with peak supraglacial discharge slightly preceding peak proglacial discharge after accounting for the -5h correction applied due to proglacial routing (**Figure 3, Table S3**).

Text S7: Computation of subglacial water storage (*S*) and subglacial water storage change (△*S*) proxies

<u>GPS-derived proxies</u>: GPS-measured vertical ice motion is a combination of three components: the vertical component of mean bed-parallel motion, vertical strain of the ice column, and vertical motion of the ice relative to the bed (due to some combination of cavity formation and till dilation, depending on basal conditions). Ideally, these components may be separated by leveraging local knowledge of ice conditions and, critically, several proximal GPS stations (e.g., *Mair et al., 2002; Anderson et al., 2004; Sugiyama and Gudmundsson, 2004; Harper et al., 2007; Howat et al., 2008; Hoffman et al., 2011; Andrews et al., 2018*). In the absence of additional GPS stations (such as for this study), the vertical strain rate cannot be estimated, but during the peak of the melt season changes in vertical strain rates are assumed, perhaps inappropriately, to be accounted for with a detrending to remove the impact of bed parallel motion, following *Bartholomew et al., (2012)* and *Cowton et al. (2016*).

As such, we detrend the 6-h smoothed z data using the linear trend of the dataset (**Figure 2c**). This limited correction introduces unquantifiable uncertainties, a particular issue with deriving uplift and basal uplift change from GPS observations. In order to calculate the rate of basal uplift, we calculate the derivative of the detrended elevation data by applying a 6-h differencing of the 15-minute dataset, as done to calculate the horizontal velocity. The detrended elevation and basal uplift rate are considered proxies for subglacial storage (*S*) and subglacial water storage change (t:*S*), respectively (**Figure 2c, Figure 5a, Figure S13a**). Our GPS-derived proxy for t:*S*, albeit noisy, presents peaks that sometimes align with short-term accelerations in ice speed (**Figure 5a, Figure S13a**), unlike our GPS-derived peaks in *S* (**Figure 2c**).

The observed lack of correlation between surface elevation and surface elevation change measurements and ice velocity are likely due, in part, to the position and nature of the GPS observations and our inability to capture sub-daily changes in vertical strain rates (**Figure S11; Table S4**). GPS-derived ice motion can be both locally and non-locally forced, particularly in ice surface depressions where moulins are often located (e.g., Price et al., 2008; *Ryser et al., 2014*). The influence of non-local forcings on our GPS elevation data is potentially evident in the GPS-derived *S* and t:*S* record. During the daily peak, there is a rapid decline and recovery, suggesting that there may be a brief period where the downstream moulin acts to longitudinally pull the upstream ice where the GPS is located, causing unaccounted for local ice thinning, before the downstream region begins to decelerate and allow the GPS-derived *S* and t:*S* signals to recover.

<u>Discharge-difference proxies:</u> While calculating basal uplift and basal uplift rates from GPS requires either multiple GPS stations or assumptions about vertical strain rate and ice flow orientation, our observations also present an opportunity to utilize an input-output approach to assess subglacial storage (*S*) and subglacial water storage change (t:*S*) more directly. Input-output methods seek to measure or estimate the discharge of surface meltwater entering a glacier or ice sheet catchment simultaneously with the discharge of proglacial water release. They have been used on smaller alpine glaciers to capture the role of subglacial water storage and change in water storage in driving short-term ice sheet motion (e.g. *Bartholomaus et al., 2008, 2011; Armstrong and Anderson, 2020*), to compute water balance of a small surface catchment in the Sermeq Avannarleq ablation zone of Greenland (*McGrath et al., 2011*), and to examine long-term storage in the Russell Glacier using surface mass balance modeling and proglacial discharge measurements (*van As et al., 2017; 2018*).

The high-quality supraglacial discharge dataset presented here (**Figure S5, Table S1, Table S2**) offers a rare in situ "input" suitable for comparison with proglacial output. Due to a large disparity between the magnitudes of supraglacial versus proglacial discharge (**Figure 2b**) the method should only be used to characterize local basal water pressure conditions near the moulin, not to make inferences about the broader subglacial region or ice edge. Within the ice sheet's broadly pressurized subglacial system (which is sourced by hundreds of moulins, see *Smith et al., 2015; Yang et al. 2016*) basal water pressures near any one moulin should be sensitive to proglacial discharge, but not the other way around. While subglacial water pressures at our study moulin should "feel" broader-scale pressure variations reflected in proglacial discharge, we do not expect proglacial discharge to be sensitive to water pressure variations introduced by any one moulin, including the one studied here.

Due to this large disparity between supraglacial and proglacial discharge, we must modify the input-output approach by using the normalized difference between measured supraglacial moulin input and proglacial discharge (**Figure 5b, 5c; Figure S13b, S13c**). To obtain a qualitative proxy for subglacial storage (*S*), we calculate the 6h cumulative input and discharge, normalize both measures of cumulative discharge (e.g. instantaneous input and output) to between 0 and 1, then calculate the difference (supraglacial minus proglacial) between these two time series (**Figure 5b; Figure S13b**). Inspection of this *S* proxy versus ice speed suggests that local subglacial storage and horizontal ice speed are offset, with ice speed peaking several hours before peak subglacial storage and weak or poor tracking in overall magnitude; however, once the derivative (t:*S*) of the proxy is calculated, the correlation with ice speed improves (**Figure 5c; Figure S11d**), especially for AK4 station (**Figure S13c, Figure S14d, Table S5**). For more about proglacial timing differences at Kangerlussuaq, AK4, and Leverett Glacier see the next section (**Text S8**).

The derivative t:*S* of the input - output storage calculation is calculated over a 6h interval, to match the same 6h position derivative used to calculate smoothed ice speed. Note that these discharge-difference calculations represent a fleeting measure of net subglacial water storage (i.e. instantaneous input minus output), not the time required for subglacial water transport. For a pressurized system like the Greenland subglacial drainage system, little or no lag is expected between a change in the rate of input and output from the system (even though individual water particles require hours to days to advect through the system). Therefore, any subglacial routing delays (which are known to range from less than 1 to multiple days in this region, *Chandler et al., 2013; van As et al., 2017*) need not be considered in meltwater *S* and t:*S* proxies. Occasional temporal offsets between our t:*S* proxy and ice speed are discussed further in **SI Text S9**.

Finally, although this paper focuses strictly on short-term behavior, our findings may have some implications for longer-term (i.e. seasonal) time scales as well. Broadly speaking, we find that meltwater-induced glacier accelerations occur when rates of supraglacial water input exceed rates of proglacial water output. Earlier in the season these imbalances may be sustained for longer when subglacial conduits are small and poorly developed, transitioning to input-output imbalances that later fluctuate around a daily mean by peak melt season (i.e. by the time of this study) when conduits are well-developed. On mountain glaciers, the response of the diurnal ice speed velocity maxima to surface melting quickens during the transition from early to peak melt season (e.g. *Armstrong and Anderson, 2020*). The process described here for Greenland thus likely varies in importance and/or intensity throughout the summer.

Text S8: Sensitivity of discharge-difference *S* and ΔS proxies to the proglacial discharge timing delay correction

Our discharge-derived subglacial storage proxies are sensitive to the proglacial timing correction applied to the Qinnguata Kuussua/Watson River proglacial discharge dataset. This effect is evident when examining correlations between ice speed with *S* and ΔS over a range of plausible time correction values (**Figure S12**). Though we apply a single, fixed -5h correction to the dataset (**see Text S6**), the real-world magnitude of the proglacial lag actually varies unpredictably, with a standard deviation of 2h (**Figure S8** and **Figure S9**). Therefore, increases in both *S* and ΔS are associated with increased ice velocity, with slight dominance of one or the other depending on choice of proglacial lag correction (see **Figure S12**). Ice speed does correlate with ΔS slightly better than *S* using the optimal -5h timing correction (see **Table S5**), but this uncertainty nonetheless makes it difficult to confidently affirm the dominance of *S* or ΔS using proglacial discharges at Kangerlussuaq bridge. The Kangerlussuaq data do, however, signify that ΔS is at least as important as *S* in driving local ice speed at our study area (r= 0.56; τ= 0.37, p<0.01 for ΔS; versus r= 0.55; τ=0.35, p>0.01 for *S*; see **Table S5**).

To eliminate need for a proglacial timing correction we also perform the same analysis comparing ice speed with discharge-difference *S* vs. ΔS using AK4 proglacial discharge measurements instead from Kangerlussuaq. Because no proglacial routing delay correction needs to be applied to the AK4 data, and because AK4 peak timing is synchronous with that of Leverett Glacier (**Figure S9**), we believe that the AK4 hydrograph may actually characterize proglacial outflow from the immediate subglacial environment better than the more distant Qinnguata Kuussua/Watson River hydrograph recorded at Kangerlussuaq, despite its small catchment size. The width of its daily peaks is narrower than would be expected for a larger catchment, resulting in double peaked behavior (**Figure S13**) that reduces the overall correlation, but ice speed nonetheless is significantly correlated with subglacial storage change ΔS calculated from AK4 data (**Figure S13, Figure S14**). Specifically, r= 0.60; τ= 0.37, p<0.01 for AK4 ΔS (but only r= 0.13; τ=0.05, p>0.01 for *S*, see **Table S5**).

Because AK4 may or may not be hydraulically connected to Rio Behar catchment (it lies at the divide between Isortoq basin and Qinnguata Kuussua/Watson River basin, landing in one basin or another depending on choice of a sensitive watershed delineation parameter threshold); and because AK4 is clearly a headwater of Qinnguata Kuussua/Watson River, we present results in the main text using Kangerlussuaq bridge data, but wish to emphasize these compelling AK4 results in SI (**Figure S13, Figure S14, Table S5**), which more compellingly show that ice speed correlates more strongly with subglacial storage rate-of-change □*S* than with storage *S*. Overall, the combined evidence from both proglacial river gauging sites (e.g. **Figure 5, Figure S11, Figure S13, Figure S14**) suggests that the classic relationship between subglacial storage change and ice motion developed for alpine glaciers (i.e. that □*S* drives short-term ice motion more than *S*) also holds for our large study catchment on the Greenland ice sheet.

Text S9: Supplemental discussion of Δ*S* proxy and ice motion

Of the variables examined here, we conclude that supraglacial river discharge is an important driver of short-term variations in ice speed at our field site, due to its influence on subglacial water storage change t:*S*. In the vicinity of the Rio Behar moulin, t:*S* is strongly paced by the integrative and delaying nature of upstream surface routing through the upstream catchment (*Smith et al., 2017*), which makes the timing of peak daily moulin input less variable than that of melt energy, air temperature, or ablation (**Figure 3**). The delay between peak melt energy and peak surface ablation has a median value of 4h, while the delay between peak surface ablation and peak moulin input has a median value of 2h (**Table S3**). Overall, instrument sensitivity made calculating short-term ablation challenging, so we applied a 6h differencing (**Text S5**), which may potentially mask the peak timing. Surface routing mitigates this variability and promotes predictable timing of melt water delivery to the moulin (e.g. *Smith et al., 2017; Yang et al. 2018; 2020*). We also note that unlike melt energy or ablation, moulin discharge does not shut down at night (**Figure 2b; Figure 4d**), possibly helping to maintain pressurized water-filled subglacial conduits and resist closure (e.g. *Bartholomaus et al., 2008; Meierbachtol et al., 2013*). The delay between peak melt energy and peak moulin input (here ~6h, **Table S3**), which reflects these surface routing delays, should therefore be carefully considered in studies of short-term ice motion variability.

Our discharge-difference proxies for *S* and t:*S* rely on a core assumption that proglacial discharges sourced from a large area of the ice sheet can reasonably characterize basal water pressure under our much smaller field site; and that supraglacial moulin inputs transfer rapidly to the bed. To use the proglacial river discharge record at Kangerlussuaq bridge we must apply a timing correction to account for the composite effects of surface flow routing and wave celerity between AK4 station and Kangerlussuaq (~33 km; **Text S6, Text S8**). No such correction is needed to create *S* and t:*S* proxies using proglacial discharges from AK4 station (**Figure S13, Figure S14, Table S5**).

While our supraglacial hydrograph and resultant qualitative t:*S* proxies appear to correlate reasonably well with ice speed (**Table S5, Figure 5c, Figure S13c**), we also note some non-linear behavior on the descending limb of diurnal peaks. A small secondary bump in ice speed and in t:*S* is noted on some days (in particular July 9, 10, 11, **Figure S13c**). There are a number of possible reasons for these phenomena. One may be that ice motion integrates both local and non-local forcings over long length scales (3-8 ice thicknesses), so ice dynamics from surrounding areas likely influence our field site. Similarly, supraglacial forcing of the subglacial system is not uniform over such length scales, with moulin inputs peaking at different times due to varying upstream catchment areas (*Smith et al., 2017; Yang et al, 2016*). While the Rio Behar moulin has no neighboring large moulins within 5 km, we cannot rule out the possibility of temporally asynchronous subglacial water delivery from nearby moulins also influencing local subglacial water storage conditions at our field site.

As described in **Text S7**, while subglacial water pressures near Rio Behar moulin are presumed sensitive to broader/regional subglacial water pressure *reflected* by proglacial outflow, we do not expect them to exert a dominant influence *upon* proglacial outflow (due to the moulin's small overall contribution to total proglacial discharge, see **Figure 2b**). We therefore maintain that our *S* and t:*S* proxies characterize subglacial conditions at the local (i.e. near the moulin), not regional scale.

Figures and Tables:

Figure S1. Photograph 1 of ADCP discharge monitoring site. A SonTek River Surveyor® M9 Acoustic Doppler Current Profiler (ADCP) mounted on a SonTek HydroBoard II being ferried across the Rio Behar supraglacial river channel cross-section in southwest Greenland (location 67.050°N, -49.018°W). The ADCP and hydroboard are tethered to a specialized bank-operated cableway developed by the field team for deployment on ice surfaces. Data relay is wireless (radio frequency). A total of 847 ADCP profiles were collected every hour for one week (5-13 July 2016). For a time-lapse camera video showing measurement collections and diurnal discharge cycles throughout the week see **Dataset S7**, **Dataset S8, Dataset S9.**

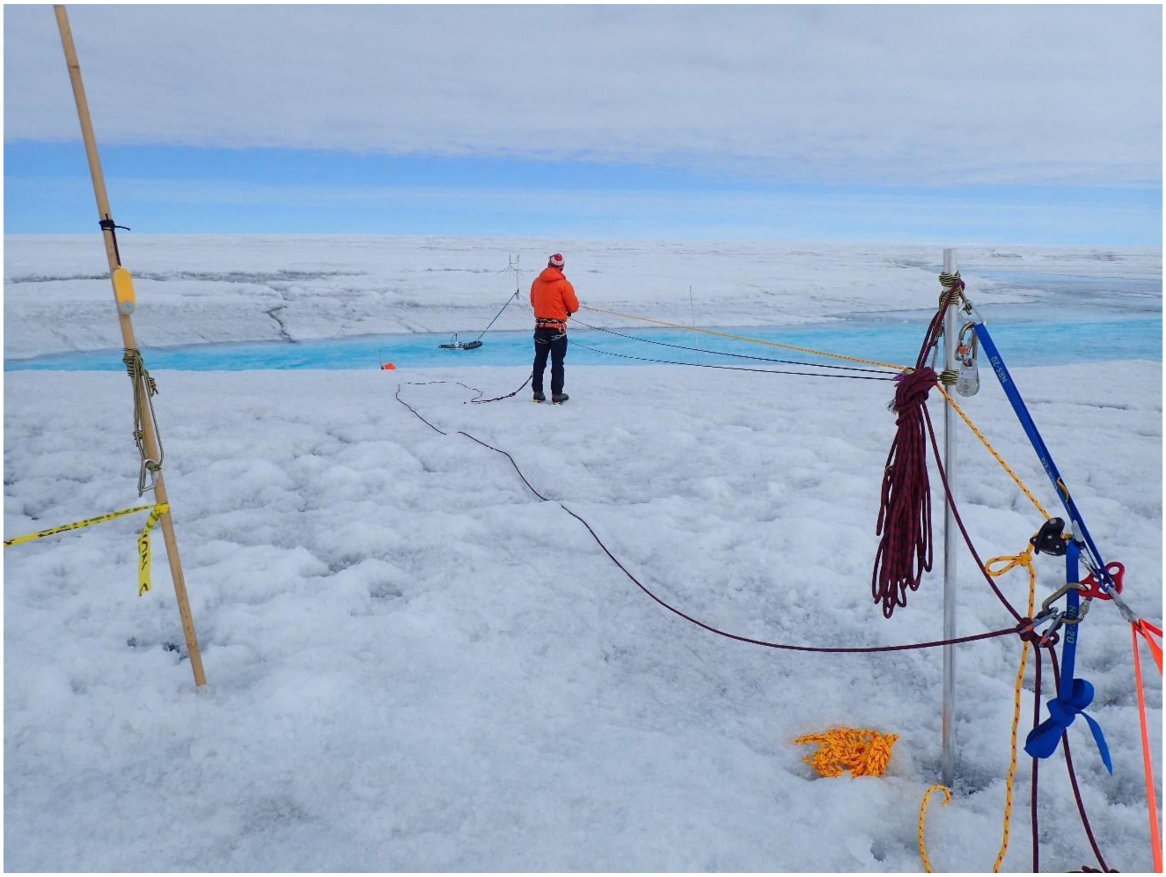

Figure S2. Photograph 2 of ADCP discharge monitoring site. The bank-operated cableway is suspended from vertical masts drilled into the ice on both banks of the supraglacial river, set back several tens of meters back from the flow. The masts support a tensioned static line and a secondary control line used by roped technicians to safely ferry the ADCP back and forth across the channel every hour.

Figure S3. Photograph 3 of ADCP discharge monitoring site. Close up photograph of the SonTek River Surveyor® M9 ADCP mounted on a SonTek HydroBoard II.

Figure S4. Photograph 4 of ADCP discharge monitoring site. Technicians controlled the ADCP instrument remotely, monitoring its data stream via radio transmissions between the instrument and a laptop computer.

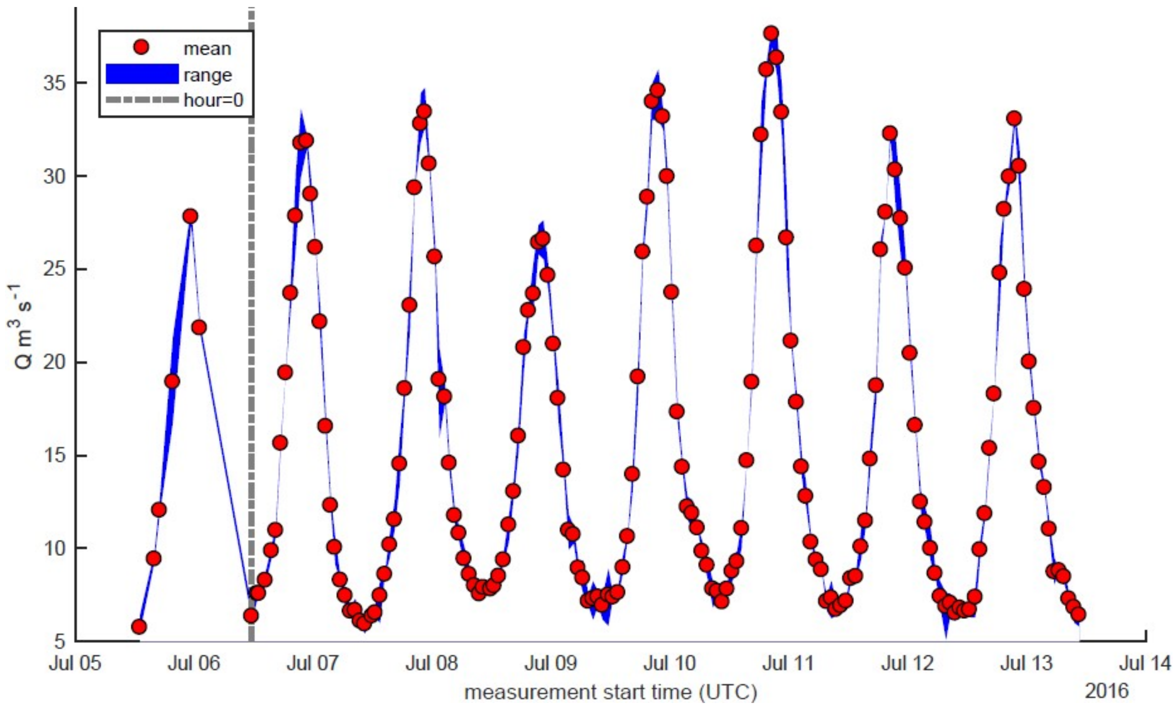

Figure S5. Hourly time-series plot of ADCP supraglacial river discharge. Time series of 174 hourly in situ discharge measurements collected at the fixed cross-section shown in **Figures S1-S4**. Out of 847 ADCP profiles collected, a total of 677 passed rigorous quality-control screening and were averaged into a 174 hourly discharge estimates. A continuous record of 168 consecutive hourly discharges commencing 11:34:50 UTC on 6 July (vertical dashed line) and concluding at 10:37:57 UTC on 13 July 2016 forms the basis of this study. Six high-quality discharge measurements acquired July 5-6 are excluded from our analysis due to their intermittency, but are included in archival data.

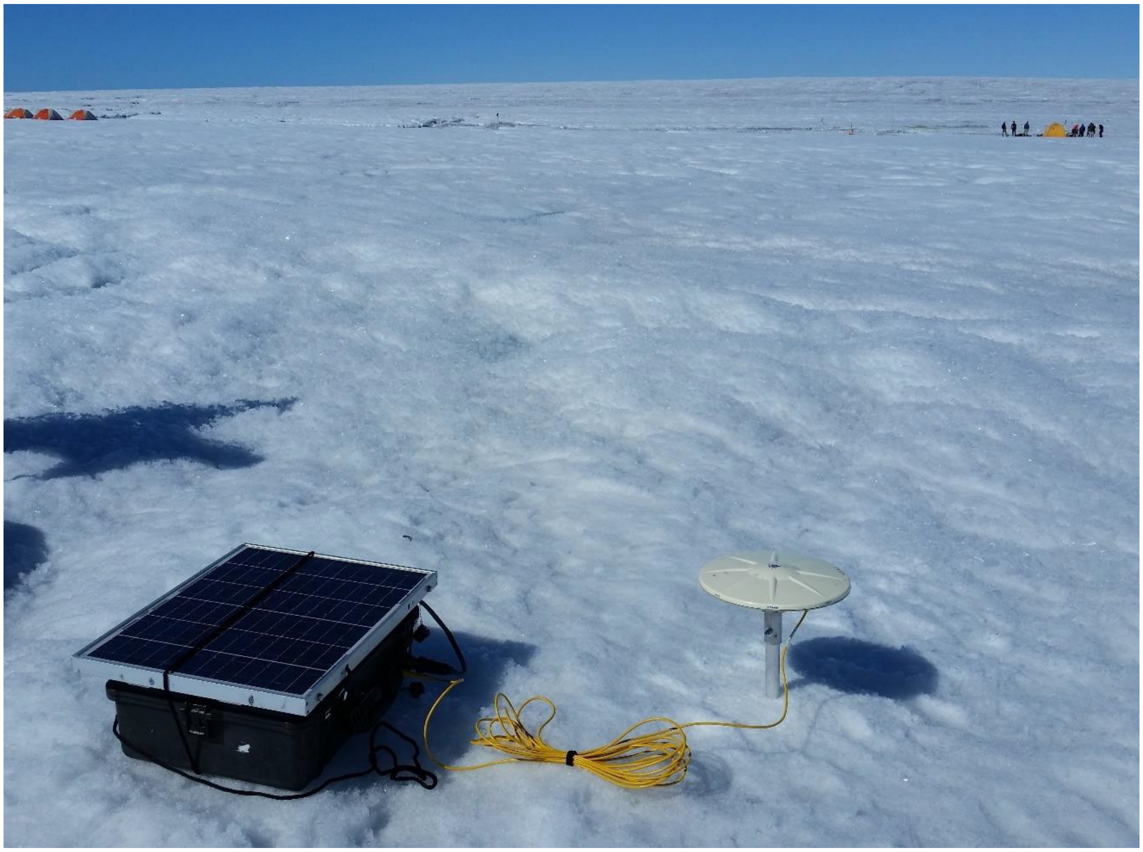

Figure S6: Photograph of GPS data collection site. Measurements of ice surface motion were collected every 5 seconds using a Trimble R7 dual-frequency global positioning system (GPS) receiver and Trimble Zephyr GPS antenna affixed to a 3.3 m schedule-40 aluminum pole drilled vertically 3 m into the ice (location 67.048°N, -49.018 °W, elevation 1211.43 m).

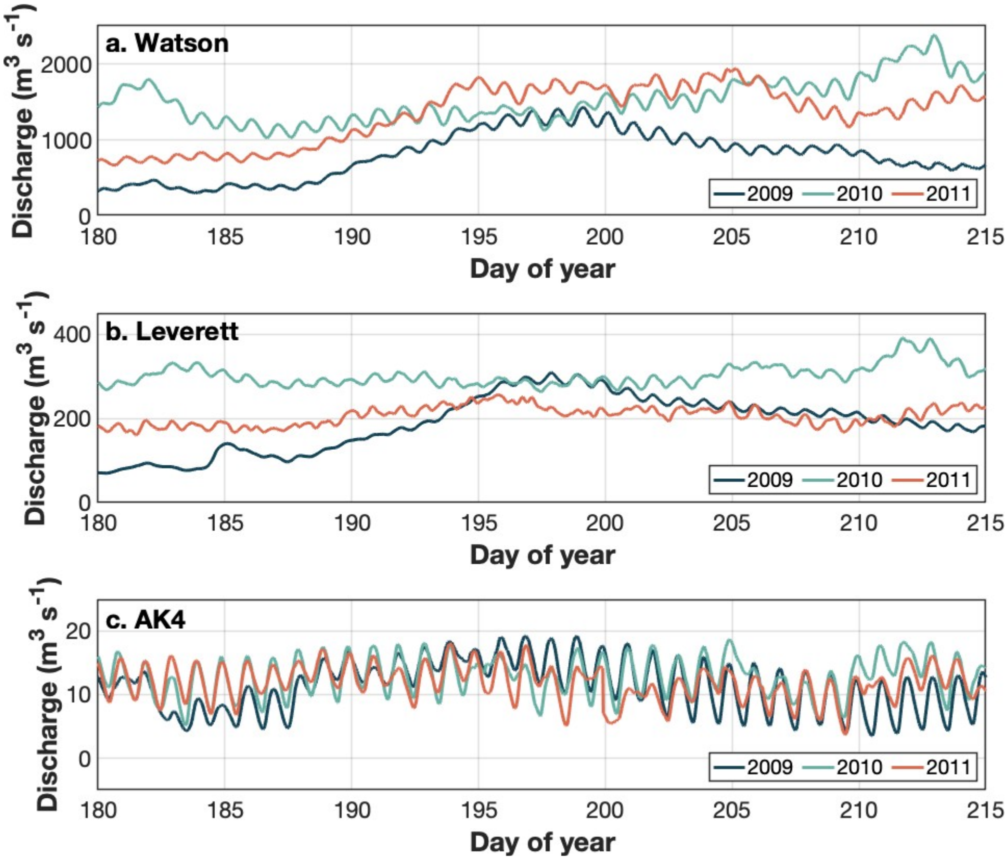

Figure S7. Proglacial discharge measurements for Qinnguata Kuussua/Watson River, AK4, and Leverett Glacier (2009-2011). Detrended discharges are shown for (a) Qinnguata Kuussua/Watson River at Kangerlussuaq bridge, (b) Leverett Glacier, and (c) Akuliarusiarsuup Kuua (AK4) during the month of July (d.o.y. 182 - 212), 2009-2011. Leverett and AK4 data have undergone initial processing to reduce the sampling interval and enhance peaks (see **Text S6**).

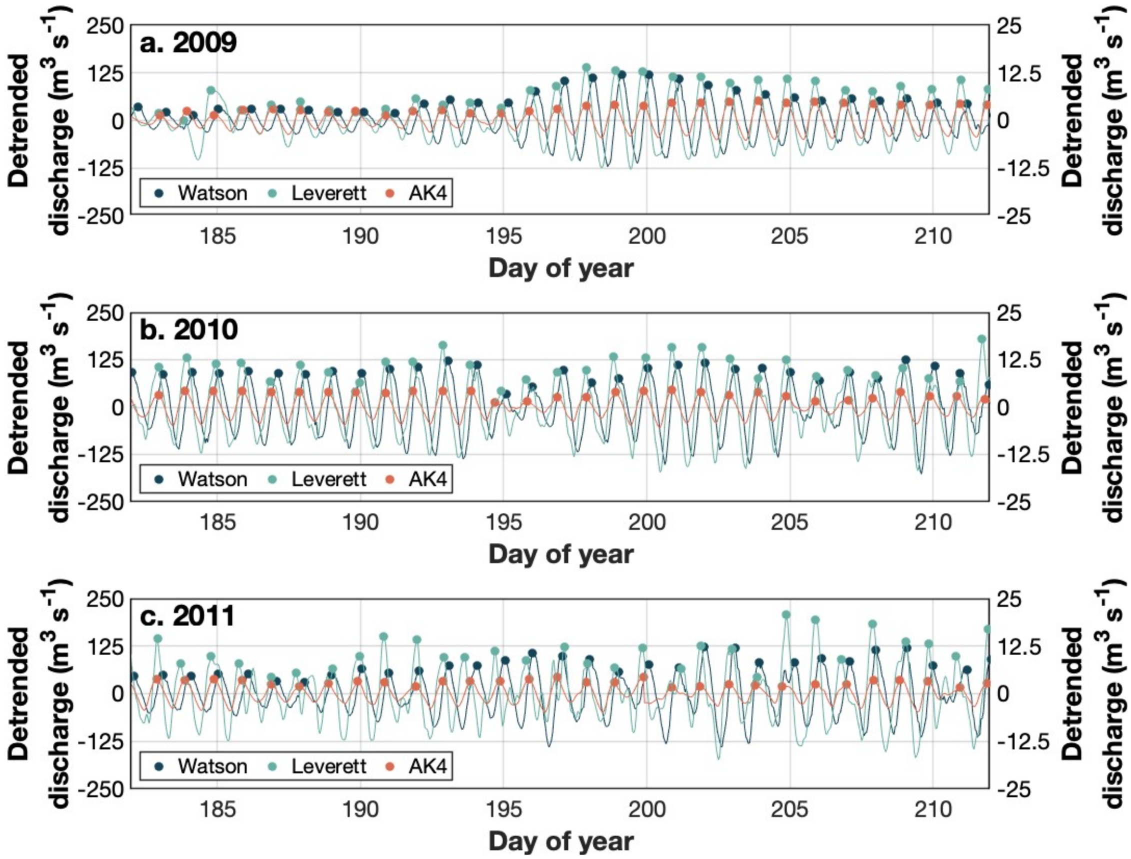

Figure S8. Detrended proglacial discharge measurements and daily peaks for Qinnguata Kuussua/Watson, AK4, and Leverett Glacier (2009-2011). Detrended discharges shown for the month of July in years (a) 2009, (b) 2010, and (c) 2011. Small circles in each panel indicate the identified daily peak. Watson data are referenced to the left y-axis and Leverett and AK4 data are referenced to the right y-axis.

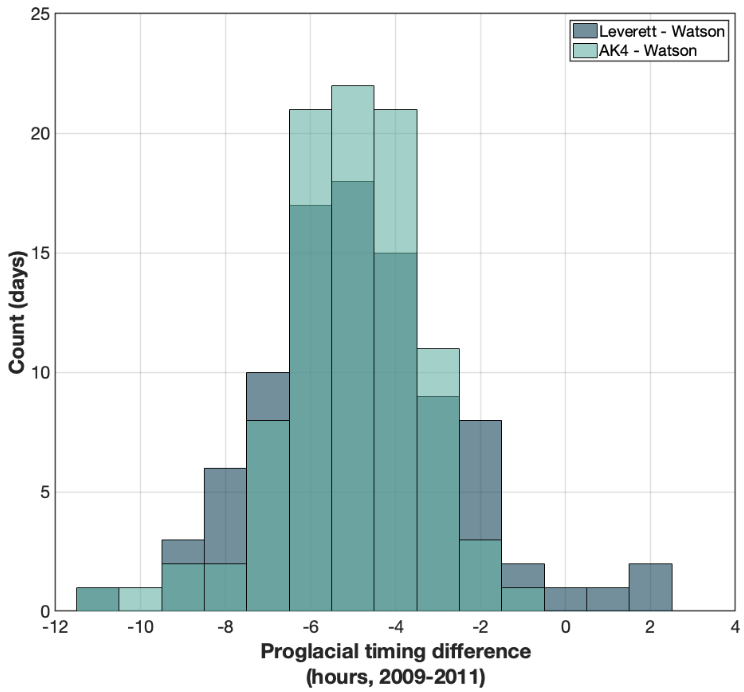

Figure S9. Distribution of daily peak timing differences for Qinnguata Kuussua/Watson - Leverett and Qinnguata Kuussua/Watson - AK4 (2009-2011). Negative values indicate that the Qinnguata Kuua/Watson River discharge peak lagged the Leverett or AK4 daily peaks.

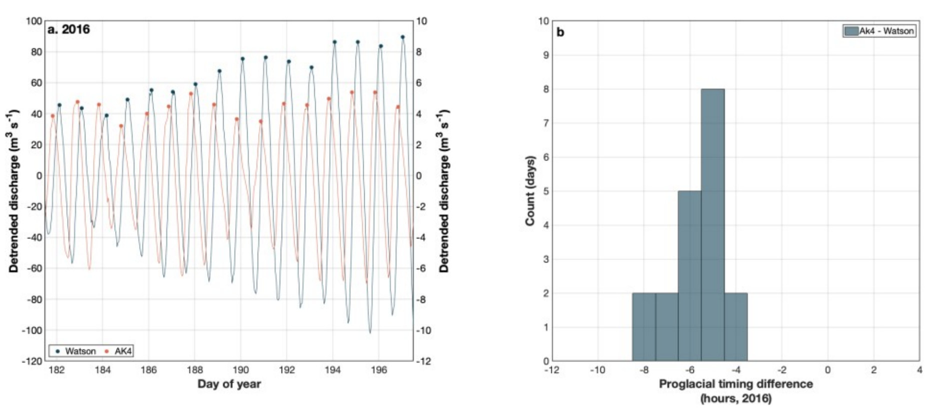

Figure S10. Detrended proglacial discharge measurements for Qinnguata Kuussua/Watson and AK4, and distribution of daily peak timing differences for Qinnguata Kuussua/Watson - AK4 (1-16 July 2016). Peak identification (a) for Watson and AK4; and (b) distribution of timing differences between Watson and AK4 daily peak discharges over the period July 1 - 16, 2016. Negative values indicate that the Watson daily peaks lagged the AK4 daily peaks.

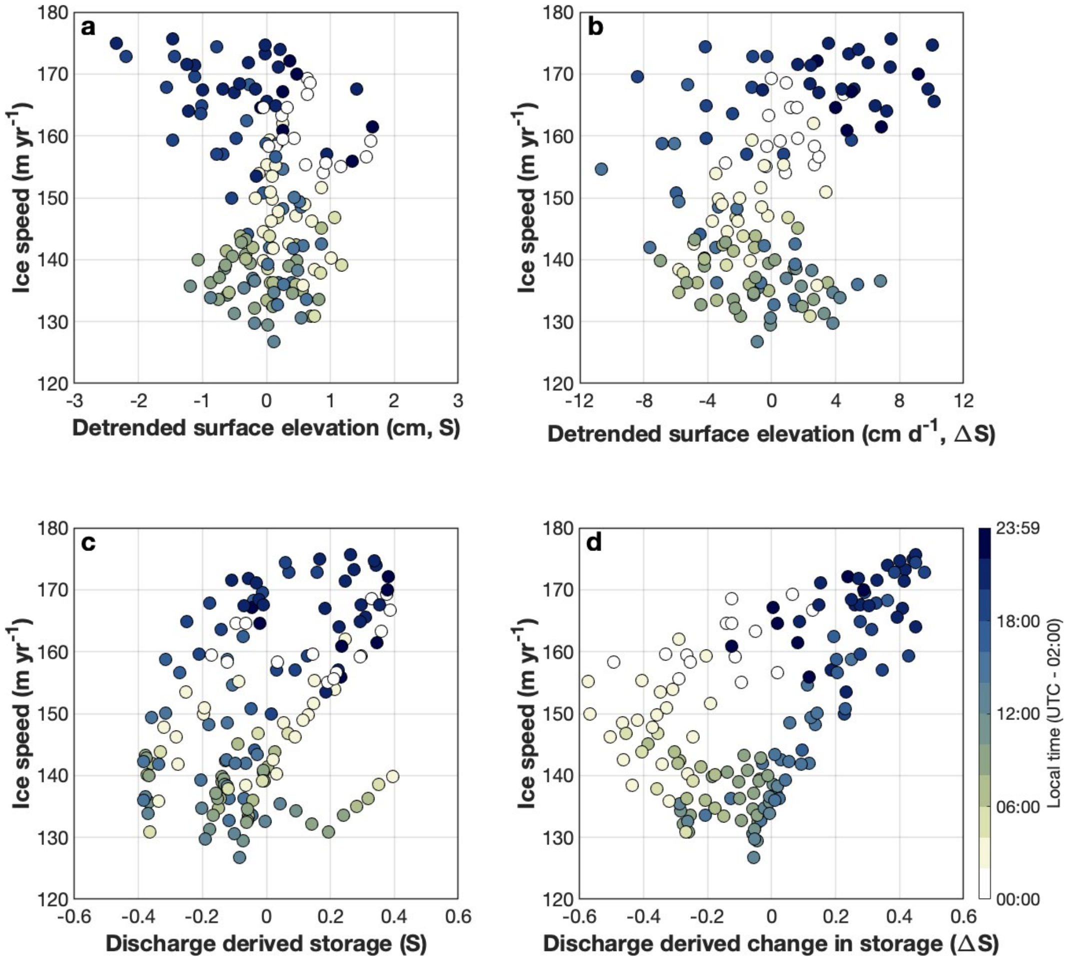

Figure S11. Correlations of horizontal ice speed with *S* and □*S* proxies computed using GPS and with Qinnguata Kuussua/Watson River proglacial discharges. Observed ice speeds compared with: (a) GPS-derived storage proxy *S* (surface elevation); (b) GPS-derived change in storage, f!.*S* (surface elevation derivative); (c) normalized discharge-difference storage proxy *S* (cumulative input-output); and (d) normalized discharge-difference change in storage proxy f!.*S* (6h input-output). Correlations use a cross-correlation value of 0 (no time offset correction to ice velocity) and a Qinnguata/Watson River proglacial timing delay correction of -5h. Corresponding Pearson *r* and Kendall rank *1″* statistical correlations are shown in **Table S5**. For a version of this figure using AK4 proglacial discharges requiring no proglacial timing correction see **Figure S14**.

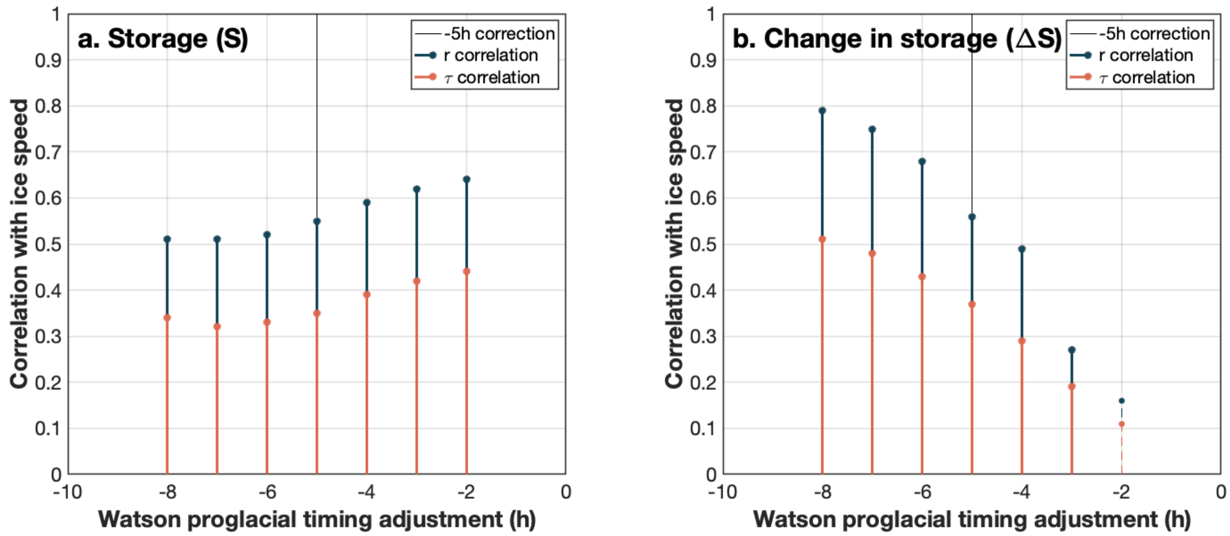

Figure S12. Sensitivity of subglacial storage proxy - ice speed correlations to choice of the Qinnguata Kuussua/Watson River proglacial timing lag correction. Pearson *r* (blue) and Kendall rank r (orange) correlation statistics between observed ice speed and (a) normalized discharge-difference subglacial storage *S*; (b) normalized discharge-difference subglacial storage change □S, associated with a range of proglacial peak timing corrections (-8h - 0h). A fixed correction of -5h (black line) was used in this study (see Figure S9). Dashed line signifies statistically insignificant correlation.

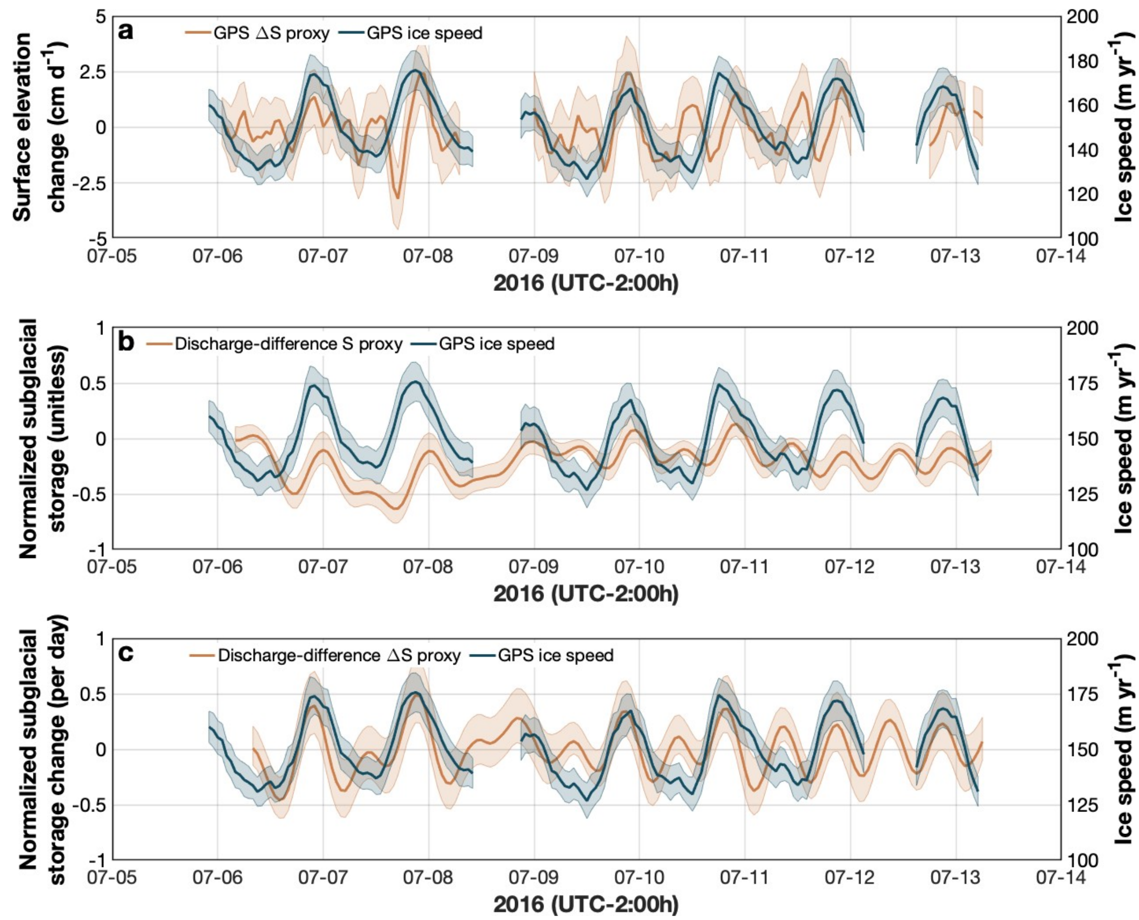

Figure S13. Comparison of horizontal ice speed with *S* and *ΔS* proxies computed using Akuliarusiarsuup Kuua (AK4) proglacial discharges. This figure is the same as **Figure 5** except uses Akuliarusiarsuup Kuua (AK4) discharge data, which require no proglacial discharge timing delay correction. Comparison of Rio Behar horizontal ice speeds (in blue) with: (a) f!.*S* as estimated from GPS-derived ice surface elevations; (b) *S* as estimated from normalized discharge-difference; (c) f!.*S* as estimated from normalized discharge-difference. f!.*S* is more strongly correlated with observed ice speed than *S* (see also **Table S5**).

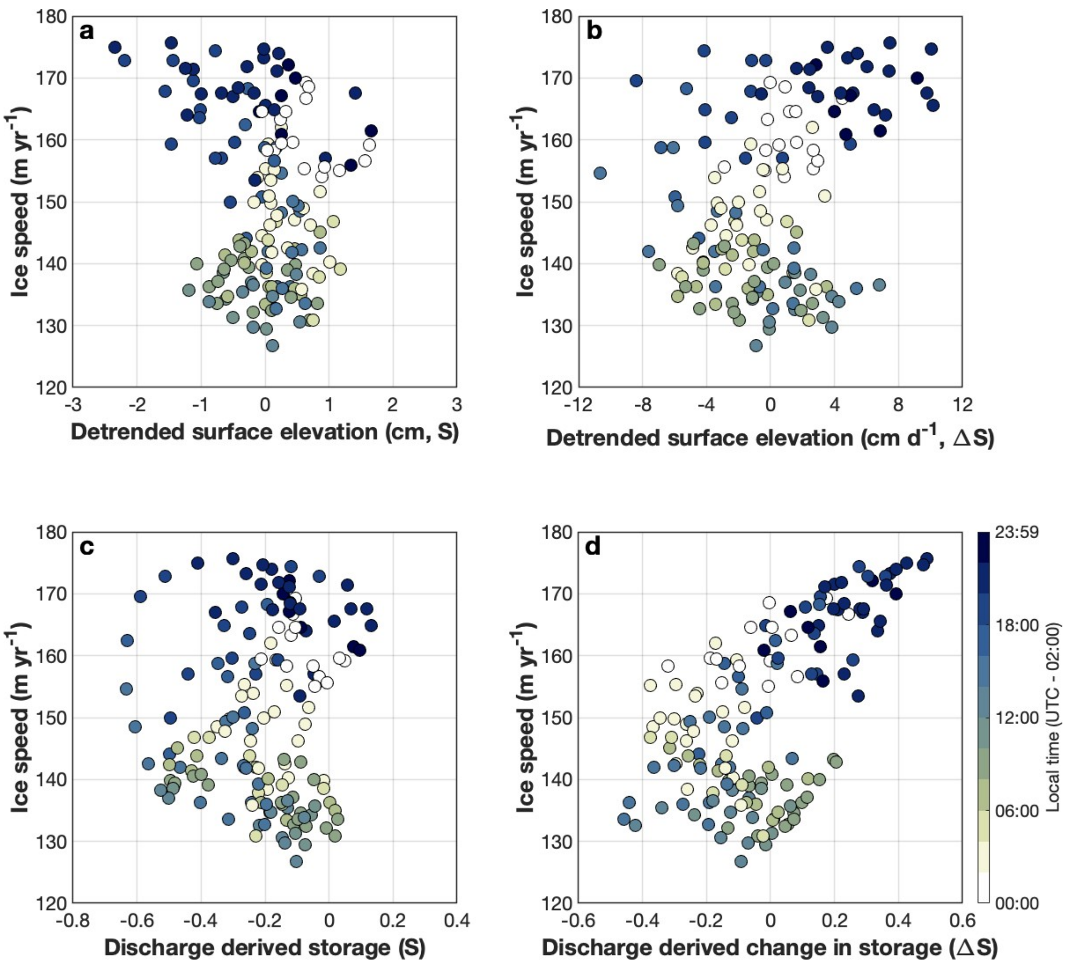

Figure S14. Correlations of horizontal ice speed with *S* and □*S* proxies computed using GPS and with Akuliarusiarsuup Kuua (AK4) proglacial discharges. This figure is the same as **Figure S11** except uses Akuliarusiarsuup Kuua (AK4) proglacial discharge data, which require no proglacial peak timing delay correction. Comparisons of ice speed with: (a) GPS-derived storage proxy *S* (surface elevation); (b) GPS-derived change in storage f!.*S* (surface elevation derivative); (c) normalized discharge-difference storage proxy *S* (cumulative input-output); and (d) normalized discharge-difference change in storage f!.*S* (6h input-output). These correlations use a cross-correlation value of 0 (no time offset correction to ice velocity) and have no proglacial timing delay correction applied. For corresponding Pearson *r* and Kendall rank *1"* correlations see **Table S5**. For a version of this figure using Qinnguata Kuussua/Watson River proglacial discharges (with a -5h timing correction applied) see **Figure S11**.

Table S1: Hourly ADCP measurements of supraglacial river discharge

n	start time (UTC)						end time (UTC)						profiles		Q m^3/s	
	yyyy	mm	dd	hr	mi	ss	yyyy	mm	dd	hr	mi	ss	total	good	avg.	std. dev.
-6	2016	7	5	13	0	9	2016	7	5	13	14	34	4	4	5.75	0.45
-5	2016	7	5	15	56	29	2016	7	5	16	3	40	4	4	9.41	0.27
-4	2016	7	5	17	0	5	2016	7	5	17	18	35	7	3	12.03	0.50
-3	2016	7	5	19	40	8	2016	7	5	19	52	46	4	3	18.93	2.34
-2	2016	7	5	23	20	5	2016	7	5	23	29	32	4	4	27.79	0.43
-1	2016	7	6	1	5	14	2016	7	6	1	14	32	4	3	21.82	0.32
0	2016	7	6	11	34	50	2016	7	6	11	43	43	4	3	6.35	0.34
1	2016	7	6	12	40	40	2016	7	6	13	0	45	7	3	7.56	0.38
2	2016	7	6	13	0	56	2016	7	6	13	40	17	7	6	7.56	0.21
3	2016	7	6	14	20	11	2016	7	6	14	31	50	6	4	8.27	0.36
4	2016	7	6	15	35	19	2016	7	6	15	45	52	6	5	9.86	0.29
5	2016	7	6	16	27	52	2016	7	6	16	40	11	6	4	10.95	0.41
6	2016	7	6	17	27	6	2016	7	6	17	35	33	4	2	15.63	0.41
7	2016	7	6	18	27	54	2016	7	6	18	41	54	5	1	19.41	0.00
8	2016	7	6	19	28	56	2016	7	6	19	49	29	7	5	23.68	0.80
9	2016	7	6	20	27	26	2016	7	6	20	37	40	4	4	27.82	1.79
10	2016	7	6	21	30	3	2016	7	6	21	47	40	6	2	31.74	2.62
11	2016	7	6	22	41	2	2016	7	6	22	51	1	4	4	31.85	0.37
12	2016	7	6	23	30	39	2016	7	6	23	50	41	6	5	29.00	0.61
13	2016	7	7	0	26	57	2016	7	7	0	37	14	4	4	26.13	0.14
14	2016	7	7	1	23	38	2016	7	7	1	31	4	4	4	22.14	0.81
15	2016	7	7	2	31	19	2016	7	7	2	40	23	5	3	16.53	0.59
16	2016	7	7	3	30	46	2016	7	7	3	38	10	4	4	12.29	0.33
17	2016	7	7	4	20	48	2016	7	7	4	27	42	4	4	10.03	0.70
18	2016	7	7	5	29	7	2016	7	7	5	35	39	4	4	8.28	0.14
19	2016	7	7	6	27	48	2016	7	7	6	34	14	4	4	7.45	0.53
20	2016	7	7	7	30	36	2016	7	7	7	36	0	4	4	6.61	0.26
21	2016	7	7	8	28	10	2016	7	7	8	37	10	6	5	6.66	0.49
22	2016	7	7	9	28	50	2016	7	7	9	34	8	4	4	6.08	0.24
23	2016	7	7	10	23	47	2016	7	7	10	42	13	9	3	5.93	0.49
24	2016	7	7	11	53	0	2016	7	7	11	58	41	4	4	6.36	0.23
25	2016	7	7	12	31	22	2016	7	7	12	38	49	4	4	6.53	0.33
26	2016	7	7	13	29	25	2016	7	7	13	41	55	6	6	7.44	0.80
27	2016	7	7	14	26	36	2016	7	7	14	34	6	5	3	8.59	0.08
28	2016	7	7	15	27	1	2016	7	7	15	40	53	7	4	10.17	0.57
29	2016	7	7	16	24	58	2016	7	7	16	36	9	6	6	11.53	0.59
30	2016	7	7	17	28	27	2016	7	7	17	42	35	6	5	14.51	1.06
31	2016	7	7	18	29	39	2016	7	7	18	38	42	4	3	18.56	0.54
32	2016	7	7	19	31	53	2016	7	7	19	44	12	6	4	23.02	1.51
33	2016	7	7	20	29	17	2016	7	7	20	41	6	6	2	29.34	0.14
34	2016	7	7	21	40	29	2016	7	7	21	58	33	8	5	32.77	1.01
35	2016	7	7	22	29	45	2016	7	7	22	43	26	4	3	33.42	1.14
36	2016	7	7	23	25	34	2016	7	7	23	34	24	4	4	30.63	0.41
37	2016	7	8	0	33	48	2016	7	8	0	41	25	4	4	25.63	0.58
38	2016	7	8	1	23	55	2016	7	8	1	30	51	4	3	19.04	2.81
39	2016	7	8	2	33	17	2016	7	8	2	40	17	4	4	18.11	0.50
40	2016	7	8	3	27	53	2016	7	8	3	34	42	4	4	14.56	0.40

41	2016	7	8	4	31	11	2016	7	8	4	36	29	4	4	11.75	0.47
42	2016	7	8	5	25	1	2016	7	8	5	31	18	4	4	10.80	0.39
43	2016	7	8	6	26	2	2016	7	8	6	35	4	6	6	9.43	0.52
44	2016	7	8	7	29	10	2016	7	8	7	34	32	4	3	8.59	0.44
45	2016	7	8	8	31	53	2016	7	8	8	36	53	4	4	7.99	0.47
46	2016	7	8	9	31	39	2016	7	8	9	39	25	6	6	7.54	0.33
47	2016	7	8	10	18	9	2016	7	8	10	30	37	6	4	7.89	0.28
48	2016	7	8	11	48	38	2016	7	8	11	59	43	7	6	7.80	0.25
49	2016	7	8	12	30	25	2016	7	8	12	41	38	6	6	7.97	0.22
50	2016	7	8	13	26	25	2016	7	8	13	36	30	6	6	8.50	0.18
51	2016	7	8	14	23	6	2016	7	8	14	30	53	4	4	9.37	0.24
52	2016	7	8	15	29	22	2016	7	8	15	36	16	4	3	11.24	0.80
53	2016	7	8	16	27	52	2016	7	8	16	34	13	4	4	13.04	0.49
54	2016	7	8	17	26	18	2016	7	8	17	35	47	4	3	16.01	0.81
55	2016	7	8	18	29	48	2016	7	8	18	38	17	4	4	20.77	0.95
56	2016	7	8	19	26	35	2016	7	8	19	38	29	6	4	22.75	0.37
57	2016	7	8	20	25	59	2016	7	8	20	35	35	6	4	23.65	1.18
58	2016	7	8	21	26	51	2016	7	8	21	37	59	4	3	26.40	0.85
59	2016	7	8	22	24	40	2016	7	8	22	35	21	6	5	26.59	0.79
60	2016	7	8	23	23	29	2016	7	8	23	32	19	4	4	24.64	0.61
61	2016	7	9	0	28	58	2016	7	9	0	36	40	4	4	20.95	0.45
62	2016	7	9	1	24	59	2016	7	9	1	37	23	6	6	18.04	0.78
63	2016	7	9	2	31	45	2016	7	9	2	37	9	4	4	14.19	0.43
64	2016	7	9	3	30	38	2016	7	9	3	36	10	4	3	10.96	1.00
65	2016	7	9	4	28	56	2016	7	9	4	34	48	4	4	10.73	0.41
66	2016	7	9	5	28	13	2016	7	9	5	33	22	4	4	8.93	0.34
67	2016	7	9	6	23	59	2016	7	9	6	30	47	6	5	8.39	0.68
68	2016	7	9	7	29	43	2016	7	9	7	37	28	6	4	7.15	0.29
69	2016	7	9	8	26	6	2016	7	9	8	34	33	6	5	7.29	0.79
70	2016	7	9	9	27	5	2016	7	9	9	34	30	6	6	7.38	0.29
71	2016	7	9	10	19	50	2016	7	9	10	29	31	6	6	6.92	0.49
72	2016	7	9	11	32	44	2016	7	9	11	43	14	7	5	7.48	1.31
73	2016	7	9	12	29	30	2016	7	9	12	35	13	4	2	7.37	0.10
74	2016	7	9	13	29	17	2016	7	9	13	35	48	4	4	7.61	0.21
75	2016	7	9	14	31	3	2016	7	9	14	39	13	6	6	8.96	0.41
76	2016	7	9	15	27	17	2016	7	9	15	35	10	4	4	10.62	0.13
77	2016	7	9	16	27	57	2016	7	9	16	33	43	4	3	13.95	0.81
78	2016	7	9	17	33	41	2016	7	9	17	39	49	4	4	19.18	0.87
79	2016	7	9	18	32	10	2016	7	9	18	42	13	6	2	25.90	0.74
80	2016	7	9	19	27	43	2016	7	9	19	35	26	4	3	28.83	0.68
81	2016	7	9	20	24	55	2016	7	9	20	36	7	7	4	33.96	0.96
82	2016	7	9	21	35	18	2016	7	9	21	48	34	6	6	34.55	1.13
83	2016	7	9	22	32	21	2016	7	9	22	41	51	4	4	33.15	0.53
84	2016	7	9	23	25	31	2016	7	9	23	41	42	5	4	29.94	0.62
85	2016	7	10	0	21	57	2016	7	10	0	32	30	4	3	23.72	0.68
86	2016	7	10	1	27	55	2016	7	10	1	37	17	4	4	17.31	0.44
87	2016	7	10	2	29	53	2016	7	10	2	36	37	4	4	14.34	0.31
88	2016	7	10	3	28	16	2016	7	10	3	35	6	4	4	12.21	0.63
89	2016	7	10	4	26	6	2016	7	10	4	35	18	6	6	11.87	0.53
90	2016	7	10	5	30	33	2016	7	10	5	35	46	4	4	11.08	0.09

91	2016	7	10	6	26	59	2016	7	10	6	31	37	4	3	9.83	0.49
92	2016	7	10	7	29	38	2016	7	10	7	35	57	6	5	9.07	0.43
93	2016	7	10	8	35	19	2016	7	10	8	42	57	6	4	7.81	0.70
94	2016	7	10	9	31	19	2016	7	10	9	36	21	4	4	7.68	0.35
95	2016	7	10	10	31	18	2016	7	10	10	36	52	4	3	7.11	0.33
96	2016	7	10	11	30	38	2016	7	10	11	36	18	4	4	7.80	0.28
97	2016	7	10	12	31	4	2016	7	10	12	47	10	6	4	8.76	0.63
98	2016	7	10	13	30	25	2016	7	10	13	38	59	4	4	9.27	0.46
99	2016	7	10	14	27	45	2016	7	10	14	39	31	6	6	11.05	0.57
100	2016	7	10	15	30	59	2016	7	10	15	37	30	4	1	14.69	0.00
101	2016	7	10	16	32	39	2016	7	10	16	46	13	6	3	18.91	0.57
102	2016	7	10	17	29	0	2016	7	10	17	37	31	4	2	26.21	0.98
103	2016	7	10	18	25	16	2016	7	10	18	36	43	6	4	32.18	1.82
104	2016	7	10	19	30	10	2016	7	10	19	53	38	5	2	35.67	0.72
105	2016	7	10	20	30	49	2016	7	10	20	46	57	6	3	37.61	0.67
106	2016	7	10	21	32	17	2016	7	10	21	46	33	6	5	36.32	1.05
107	2016	7	10	22	32	17	2016	7	10	22	45	26	6	5	33.39	1.04
108	2016	7	10	23	31	16	2016	7	10	23	43	50	6	6	26.65	1.53
109	2016	7	11	0	26	6	2016	7	11	0	33	13	4	2	21.11	0.45
110	2016	7	11	1	31	25	2016	7	11	1	37	40	4	4	17.83	0.46
111	2016	7	11	2	32	23	2016	7	11	2	37	32	4	4	14.36	0.57
112	2016	7	11	3	24	39	2016	7	11	3	30	35	4	4	12.78	0.57
113	2016	7	11	4	26	20	2016	7	11	4	32	21	4	3	10.32	0.20
114	2016	7	11	5	29	27	2016	7	11	5	35	56	6	4	9.36	0.24
115	2016	7	11	6	32	27	2016	7	11	6	36	8	4	3	8.84	0.08
116	2016	7	11	7	34	32	2016	7	11	7	39	31	4	4	7.13	0.35
117	2016	7	11	8	31	47	2016	7	11	8	38	32	6	6	7.32	0.72
118	2016	7	11	9	29	45	2016	7	11	9	35	1	4	2	6.70	0.45
119	2016	7	11	10	27	28	2016	7	11	10	31	55	4	4	6.90	0.31
120	2016	7	11	11	32	9	2016	7	11	11	37	17	4	4	7.15	0.31
121	2016	7	11	12	27	52	2016	7	11	12	39	32	8	5	8.36	0.18
122	2016	7	11	13	29	41	2016	7	11	13	36	15	6	5	8.48	0.25
123	2016	7	11	14	31	48	2016	7	11	14	39	35	6	6	10.07	0.64
124	2016	7	11	15	28	23	2016	7	11	15	33	27	4	3	11.45	0.40
125	2016	7	11	16	25	7	2016	7	11	16	30	31	4	4	14.78	0.66
126	2016	7	11	17	37	30	2016	7	11	17	44	18	4	2	18.72	1.04
127	2016	7	11	18	30	41	2016	7	11	18	38	32	4	2	26.01	0.86
128	2016	7	11	19	30	57	2016	7	11	19	39	51	4	1	28.02	0.00
129	2016	7	11	20	28	57	2016	7	11	20	35	24	4	2	32.24	0.71
130	2016	7	11	21	26	31	2016	7	11	21	36	48	6	5	30.30	1.57
131	2016	7	11	22	32	25	2016	7	11	22	38	28	4	4	27.69	1.56
132	2016	7	11	23	29	38	2016	7	11	23	37	52	4	4	25.02	0.47
133	2016	7	12	0	27	7	2016	7	12	0	32	24	4	4	20.45	0.61
134	2016	7	12	1	29	7	2016	7	12	1	35	21	4	3	16.58	0.31
135	2016	7	12	2	32	15	2016	7	12	2	50	37	8	4	12.47	0.59
136	2016	7	12	3	28	0	2016	7	12	3	33	16	4	4	11.38	0.59
137	2016	7	12	4	34	8	2016	7	12	4	41	30	4	4	9.98	0.74
138	2016	7	12	5	29	7	2016	7	12	5	34	11	4	4	8.64	0.22
139	2016	7	12	6	30	41	2016	7	12	6	35	39	4	4	7.40	0.66
140	2016	7	12	7	37	46	2016	7	12	7	45	29	8	5	6.87	1.09

141	2016	7	12	8	32	14	2016	7	12	8	36	53	4	3	7.05	0.65
142	2016	7	12	9	30	47	2016	7	12	9	37	26	6	5	6.51	0.35
143	2016	7	12	10	30	26	2016	7	12	10	35	37	4	4	6.78	0.17
144	2016	7	12	11	27	26	2016	7	12	11	31	30	4	4	6.62	0.25
145	2016	7	12	12	25	32	2016	7	12	12	33	24	5	4	6.69	0.40
146	2016	7	12	13	35	28	2016	7	12	13	41	13	4	4	7.37	0.75
147	2016	7	12	14	31	55	2016	7	12	14	37	28	4	3	9.91	0.49
148	2016	7	12	15	32	50	2016	7	12	15	38	11	4	4	11.85	0.25
149	2016	7	12	16	29	55	2016	7	12	16	36	7	4	4	15.35	0.39
150	2016	7	12	17	25	0	2016	7	12	17	30	24	4	1	18.27	0.00
151	2016	7	12	18	33	56	2016	7	12	18	48	24	5	3	24.76	1.68
152	2016	7	12	19	26	49	2016	7	12	19	33	27	4	2	28.18	0.29
153	2016	7	12	20	26	29	2016	7	12	20	33	39	4	2	29.93	1.02
154	2016	7	12	21	33	11	2016	7	12	21	39	21	4	2	33.04	0.62
155	2016	7	12	22	27	30	2016	7	12	22	33	23	4	4	30.50	1.19
156	2016	7	12	23	32	6	2016	7	12	23	40	37	4	3	23.89	0.62
157	2016	7	13	0	29	22	2016	7	13	0	39	31	6	5	20.00	0.41
158	2016	7	13	1	26	47	2016	7	13	1	35	10	5	3	17.50	0.42
159	2016	7	13	2	28	39	2016	7	13	2	32	31	3	3	14.62	0.43
160	2016	7	13	3	32	11	2016	7	13	3	39	26	5	4	13.25	0.21
161	2016	7	13	4	31	1	2016	7	13	4	37	1	4	3	11.02	0.45
162	2016	7	13	5	28	53	2016	7	13	5	33	31	4	4	8.73	0.73
163	2016	7	13	6	29	41	2016	7	13	6	34	5	4	2	8.79	0.01
164	2016	7	13	7	27	44	2016	7	13	7	34	29	6	5	8.46	0.34
165	2016	7	13	8	28	1	2016	7	13	8	32	10	4	3	7.28	0.24
166	2016	7	13	9	29	48	2016	7	13	9	39	25	6	6	6.82	0.53
167	2016	7	13	10	31	5	2016	7	13	10	37	57	6	6	6.41	0.41

Legend:

n - measurement number (-6 to 167, 174 total measurements)

yyyy - year

mm - month

dd - day

hr - hour (UTC)

mi - minute (UTC)

ss - second (UTC)

total - number of ADCP profiles collected during a measurement

good - number of ADCP profiles flagged as usable during QA/QC for a measurement

avg. - average of all usable ADCP profiles for a measurement. Units = m^3/s

st. dev. - standard deviation of all usable ADCP profiles for a measurement

Table S2. Minimum, maximum and diurnal range of ADCP supraglacial river discharge

Time			**n** per	**Minimum**			**Maximum**			**Diurnal Range**	
yyyy	mm	dd	day	n	hh	Q m³/s	n	hh	Q m³/s	hours	Q m³/s
2016	7	5	5	-6	13	5.75	-2	23	27.79	-	-
2016	7	6	14	0	11	6.35	11	22	31.85	-	-
2016	7	7	24	23	10	5.93	35	22	33.42	12	27.49
2016	7	8	24	46	9	7.54	59	22	26.59	13	19.05
2016	7	9	24	71	10	6.92	82	21	34.55	11	27.63
2016	7	10	24	95	10	7.11	105	20	37.61	10	30.50
2016	7	11	24	118	9	6.70	129	20	32.24	11	25.53
2016	7	12	24	142	9	6.51	154	21	33.04	12	26.53
2016	7	13	11	167	10	6.41	157	0	20.00	-	-
minimum*						5.93			26.59		19.05
maximum*						7.54			37.61		30.50

Legend:

yyyy - year of measurement

mm - month of measurement

dd - start day of measurement

hh - start hour of measurement (UTC)

n per day - number of measurements per calendar day

n - measurement number (-6 to 167, 174 total measurements)

* calculated on calendar days with continuous hourly measurement measurements for each calendar day

Table S3. Daily median peak timing, mean value, and normalized prominence of study variables (peak times are rounded to nearest 1h). Normalized prominence values closer to 1 indicate a clear, strong peak, while values closer to 0 indicate noisy data with hard-to-discern peaks.

Variable	**Median peak time (UTC-2h)**	**Maximum peak time (UTC-2h)**	**Minimum peak time (UTC-2h)**	**Mean value**	**Mean normalized peak prominence**
Air Temperature (°C)	14:00	18:00	13:00	1.25	0.54
Melt energy (W m^2)	14:00	15:00	13:00	390.70	0.90
Ice surface ablation (cm d^{-1})	18:00	19:00	14:00	16.28	0.74
Moulin input (m^3 s^{-1})	20:00	21:00	19:00	32.22	0.77
Ice speed (m yr^{-1})	21:00	22:00	18:00	169.82	0.72
Detrended surface elevation (cm)	00:00*	05:00*	23:00	1.00	0.39
Detrended proglacial discharge (m^3 s^{-1})	19:00	19:00	19:00	78.08	0.61

*Best correlated peak occurred the following day

Table S4. Statistical correlations (Kendall rank *τ* and Pearson *r* values) between ice speed (time-shifted) and potential subglacial forcing parameters.

Potential supraglacial forcing variable	Ice speed time shift (h)	Kendall rank correlation[1]		Pearson *r* correlation[2]	
		r	p-value	*r*	p-value
Melt energy	-7	0.67	<0.01	0.90	<0.01
Air temperature	-8	0.54	<0.01	0.70	<0.01
Ice surface ablation	-4	0.59	<0.01	0.74	<0.01
Moulin input	-2	0.70	<0.01	0.90	<0.01
Detrended proglacial discharge[3]	-2	0.71	<0.01	0.88	<0.01
Detrended ice surface elevation	6	0.24	<0.01	0.36	<0.01

[1]Burkey (2021)
[2]Matlab `corrcoef`
[3]Qinnguata Kuussua/Watson River at Kangerlussuaq

Table S5. Statistical correlations (Kendall rank *τ* and Pearson *r* values) between ice speed and potential subglacial forcing parameters.

Potential subglacial forcing variable	Kendall rank correlation[1]		Pearson *r* correlation[2]	
	r	p-value	*r*	p-value
GPS-derived storage (*S*)	-0.08	0.13	-0.20	0.01
GPS-derived change in storage (Δ*S*)	0.16	<0.01	0.29	<0.01
normalized discharge-difference storage proxy (*S*, Watson)	0.35	<0.01	0.55	<0.01
normalized discharge-difference change in storage proxy (Δ*S*, Watson)	0.37	<0.01	0.56	<0.01
normalized discharge-difference storage proxy (*S*, AK4)	0.05	0.43	0.13	0.13
normalized discharge-difference change in storage proxy (Δ*S*, AK4)	0.37	<0.01	0.60	<0.01

[1]Burkey (2021)
[2]Matlab `corrcoef`

Dataset Captions:

Data Set S1. Summary data tables (hourly and daily) for Acoustic Doppler Current Profiler (ADCP) supraglacial river discharge measurements, acquired 5-13 July 2017 (Excel spreadsheet format)

Data Set S2. Summary data (hourly) for Acoustic Doppler Current Profiler (ADCP) supraglacial river discharge measurements, acquired 5-13 July 2017 (Plain Text format)

Data Set S3. Hourly air temperature, melt energy and ice surface ablation time series computed from PROMICE KAN-M Automated Weather Station measurements, July 2016

Data Set S4. GPS-derived ice surface positions, uncertainties, and 6h ice speed calculations, acquired 5-13 July 2016

Data Set S5. Proglacial river discharges and calculations for Qinnguata Kuussua/Watson River (Kangerlussuaq), Akuliarusiarsuup Kuua (AK4), and Leverett Glacier gauging stations

Data Set S6. Hourly GPS-derived and discharge-difference proxies for subglacial storage (*S*) and subglacial storage change (f!.*S*), including uncertainties, calculated for 6-13 July 2016

Data Set S7. Time-lapse camera video (15 minute sampling) of Rio Behar water level fluctuations and ADCP data collections at our discharge monitoring site (.mp4 format)

Data Set S8. Time-lapse camera video (15 minute sampling) of Rio Behar water level fluctuations and ADCP data collections at our discharge monitoring site (.avi format)

Data Set S9. Time-lapse camera video (5 minute sampling) of Rio Behar water level fluctuations and ADCP data collections at our discharge monitoring site (.avi format)